Separation and Purification Technology 391 (2026) 137073

Contents lists available at ScienceDirect

Separation and Purification Technology

journal homepage: www.elsevier.com/locate/seppur

Design of a hierarchical MXene-reduced graphene oxide-modified electrode decorated with layered double hydroxide for treatment of perfluorooctanoic acid (PFOA) in aqueous solution

Zhang Xinxiang [a,b], Yu Hai [b], Gao Wenzheng [b], Zhang Manyi [b], Lou Zhengzheng [c], He Li [d], Li Weidong [a,*], Shatha A. Aldaghfag [e], Kamaliddin Abdivakhidov [f], Ruslanbek Siddikov [g], Reda A. Haggam [h,*]

[a] School of Engineering, Hangzhou Normal University, Hangzhou 310018, China
[b] Zhejiang Province Environmental Engineering Co., Ltd, Hangzhou 310012, China
[c] Hangzhou Hengjun Environmental Engineering Co., Ltd, Hangzhou 310063, China
[d] Zhejiang Carbon Reduction Technology Co., Ltd, Hangzhou 310015, China
[e] Department of Physics, College of Sciences, Princess Nourah bint Abdulrahman University, P. O. Box 84428, Riyadh 11671, Saudi Arabia
[f] Kimyo International University in Tashkent, Shota Rustaveli str. 156, Tashkent 100121, Uzbekistan
[g] Urgench State University, 14, Kh. Alimdjan str, Urgench 220100, Uzbekistan
[h] Department of Chemistry, Faculty of Science, Islamic University of Madinah, Madinah 42351, Saudi Arabia

ARTICLE INFO

Editor: Philiswa Nomngongo

Keywords:
Per- and polyfluoroalkyl
Electroadsorption
MXene
Graphene oxide
NiFe-LDH

ABSTRACT

Per- and polyfluoroalkyl substances (PFAS) are persistent aquatic contaminants that demand efficient, regenerable removal technologies. Here, we report a MXene-based electroadsorbent in which delaminated $Ti_3C_2T_x$ is spaced by reduced graphene oxide (rGO) and conformally coated with NiFe layered double hydroxide (LDH) to form a MXene@rGO–LDH electrode (MGL). Adsorption kinetics follow a pseudo-second-order model, with MGL exhibiting the fastest uptake and an initial rate of 15.93 mg g^{-1} min^{-1}. Equilibrium is well described by the Langmuir model with a maximum capacity of 119.52 mg g^{-1} for MGL, outperforming MXene (64.55 mg g^{-1}). Moreover, high removal is maintained across a broad pH range, peaking at pH 4 (98.45%) and remaining substantial at pH 10 (86.39%) under closed-circuit operation. However, open-circuit conditions lead to markedly lower efficiency (80.51% to 49.35%), highlighting the role of the applied electric field. Furthermore, the electrode performs best at 1 mM $NaNO_3$ and retains tolerance toward natural organic matter (56% removal at 10 mg L^{-1} humic acid). Additionally, regeneration by reverse bias in an ethanol/$NaNO_3$ eluent enables ~70% performance retention after 10 cycles. Post-cycling SEM, XRD, and XPS were conducted to directly verify the structural and chemical stability of the MGL-3 electrode after repeated electroadsorption/regeneration. In addition, XPS was also employed to elucidate the PFOA electroadsorption mechanism by tracking adsorption-induced changes in surface bonding/chemical states under the applied bias. Thus, integrating rGO spacing with LDH functionalization on MXene yields a high-surface-area, fast-kinetic electroadsorbent that achieves competitive PFAS removal at modest bias.

1. Introduction

Global water security is increasingly constrained not only by physical shortages but also by quality degradation that renders available resources unfit or costly to use [1,2]. United Nations figs. (2018) indicate that more than 2.2 billion people still lack safely managed drinking water. More recent projections warn that up to 2.4 billion urban residents could face water scarcity [3]. Pollutants that persist in the environment, such as legacy organic contaminants, pharmaceuticals, microplastics, and heavy metals, accumulate in surface and groundwater, elevate treatment complexity and cost [4]. This quality-driven scarcity compounds drought, over-abstraction, and climate variability, intensifying pressures on utilities and ecosystems and underscoring the need for treatment technologies that can restore impaired supplies at

* Corresponding authors.
E-mail addresses: lwd@hznu.edu.cn (L. Weidong), relhaggan@iu.edu.sa (R.A. Haggam).

https://doi.org/10.1016/j.seppur.2026.137073
Received 14 December 2025; Received in revised form 23 January 2026; Accepted 28 January 2026
Available online 29 January 2026

scale.

Per- and polyfluoroalkyl substances (PFAS) are synthetic surfactants and polymers with densely fluorinated carbon chains [5]. Their strong C—F bonds make them thermally and chemically persistent, resisting hydrolysis, photolysis, and biodegradation [6,7]. Moreover, perfluorooctanoic acid (PFOA), a legacy perfluorinated carboxylate, is a strong acid that occurs predominantly as the perfluorooctanoate anion in water. It is highly soluble and mobile, facilitating long-range transport in surface and groundwater [8]. Contemporary water treatment therefore relies on two categories. First, separation technologies, including granular activated carbon [9], anion-exchange resins [10], and pressure membranes [11], which can capture a wide range of PFAS but generate secondary waste streams (spent media or brines). Second, destructive approaches, like electrochemical oxidation [12], advanced oxidation/reduction [13], and emerging plasma methods [14], that aim to defluorinate to inorganic fluoride but often face energy, matrix-interference, or by-product control challenges.

Among available treatment options, adsorption is especially attractive because it is simple to operate, scalable, energy-efficient, and compatible with existing water-treatment trains. It can also be tailored for selectivity through surface chemistry and pore design. Nevertheless, many common adsorbents, including activated carbon [15], molecularly imprinted polymers [16], anion-exchange resins [17], and various synthetics [18], show slow uptake and modest capacities at trace concentrations. As a result, high sorbent dosages or elevated influent levels are often required to reach targets. To address these adsorption limitations, electroadsorption couples a conductive sorbent with a modest applied potential to actively concentrate anions at the electrode's electric double layer and, in some systems, engage redox-inactive pseudocapacitive sites [19]. This voltage control accelerates mass transfer, enhances capacity at low concentrations, and enables on-demand regeneration by polarity reversal with minimal secondary waste [20]. For PFAS treatment, success depends on engineered composites that combine robust conductivity with positively charged and hydrophobic domains to achieve trace-level capture and efficient cycling [21].

To synthesize an effective engineered electrode for electroadsorption, it is essential to select supports that combine high electronic conductivity with large, accessible surface area [22]. MXenes (e.g., $Ti_3C_2T_x$) are attractive because they offer metallic-level conductivity, high interfacial capacitance, and tunable surface terminations that enable rapid, voltage-driven anion enrichment [23,24]. However, pristine MXenes tend to restack, are prone to aqueous/oxygen-induced oxidation, and show limited interaction with hydrophobic fluorinated chains [25], factors that depress capacity and cycling stability [26–28]. Incorporating graphene oxide (GO) or reduced GO (rGO) addresses these issues by spacing MXene sheets, establishing continuous ion/electron pathways, and introducing π-rich hydrophobic domains. Moreover, rGO further restores high conductivity and mechanical robustness. As a result, MXene-based composites implement the required features for PFAS electroadsorption [29].

Layered double hydroxides (LDHs), especially transition-metal hydroxides, are well suited to upgrade MXene@rGO electrodes for electroadsorption. Their positively charged brucite-like layers and exchangeable interlayers provide dense, accessible anion-binding sites that complement the conductivity and hydrophobic domains of MXene@rGO, enabling stronger capture of perfluorinated carboxylates under a modest positive bias [30]. As ultrathin nanosheets, LDHs disperse over the MXene@rGO scaffold to create hierarchical porosity, suppress MXene restacking, and add redox-inactive pseudocapacitance that accelerates ion uptake at trace concentrations.

Despite rapid progress, key gaps remain in the literature. Most studies emphasize passive adsorption or single-component electrodes, with limited performance at trace concentrations, incomplete regeneration metrics, and insufficient durability under realistic matrices. Systematic strategies that co-integrate high conductivity, accessible positive charge, and hydrophobic domains in a single, hierarchically porous electrode are still scarce. Notably, we found no prior reports on MXene@rGO or MXene@rGO–LDH electrodes specifically designed and evaluated for electroadsorption of PFAS/PFOA.

In this study, we synthesize a series of MXene@rGO (MG) by varying the rGO weight fraction and, from the best MG, construct ternary hierarchical MXene@rGO–LDH (MGL) by in-situ growth of NiFe layered double hydroxide. In this manuscript, hierarchical describes a deliberately engineered multi-level electrode architecture spanning multiple length scales. Specifically, the electrode integrates a microscale carbon-cloth current collector, a lamellar 2D MXene@rGO framework that forms interconnected ion-transport channels, and nanoscale NiFe-LDH sheets conformally anchored on the scaffold to maximize accessible surface sites. Structural and chemical characterization includes XRD, Raman, XPS, N_2 sorption (BET), and electron microscopy (SEM/TEM). Electrochemical behavior is examined by cyclic voltammetry and impedance spectroscopy to assess conductivity and interfacial charge storage. Moreover, the PFOA electroadsorption was evaluated under different conditions, including various pH, ionic strength, applied potential, and coexisting natural organic matter (humic acid). Furthermore, uptake is analyzed with pseudo-first-order, pseudo-second-order, Elovich, and intraparticle-diffusion kinetics, plus Langmuir, Freundlich, Temkin, and Dubinin–Radushkevich isotherms. Finally, the mechanism is evaluated by XPS before and after exposure.

2. Material and methods

2.1. Materials

Details of materials, grades, and handling are provided in Text S1 of Supporting Information (SI).

2.2. Synthesis of delaminated $Ti_3C_2T_x$ MXene

Delaminated $Ti_3C_2T_x$ was prepared from Ti_3AlC_2 (MAX) using the LiF/HCl route that generates HF in situ. LiF was dissolved in 9 M HCl in PTFE vessels held in an ice bath, and Ti_3AlC_2 powder was introduced gradually under stirring. The slurry was maintained at 35 °C for 24 h, after which the etched solid was isolated by centrifugation and washed repeatedly with deionized water until the supernatant reached pH ~6. Intercalation with 0.5 M DMSO facilitated delamination; a brief sonication on ice afforded a stable colloid of few-layer $Ti_3C_2T_x$ [31].

2.3. Preparation of the MXene@rGO scaffold

Delaminated $Ti_3C_2T_x$ was combined with GO to prepare three MXene:rGO mass ratios, including 95:5, 90:10, and 85:15, via in-situ reduction. For each composition, GO was added to yield the target MXene:rGO ratio after reduction. 15 mM of L-ascorbic acid was added, and the suspension was heated at 85 °C for 2 h under gentle stirring with a loose cap to reduce GO to rGO while maintaining intimate mixing with $Ti_3C_2T_x$. The dispersion was cooled to room temperature, washed three times by centrifugation and redispersion in deoxygenated water to remove residual reductant and salts. Films were cast on the current collector and dried at 55 °C under N_2. The final composites are denoted MG-5, MG-10, and MG-15 [32].

2.4. Fabrication of MXene@rGO films on carbon cloth

Carbon cloth (woven carbon fiber current collector) was cleaned by ultrasonication in acetone, ethanol, and water, air-dried, and briefly heated at 80 °C. The MXene@rGO was deposited by vacuum filtration onto a masked geometric area. Coated substrates were dried at 60 °C under N_2 to minimize $Ti_3C_2T_x$ oxidation. Finally, a short hot-press at 80 °C under modest pressure was used to improve interfacial contact while preserving porosity.

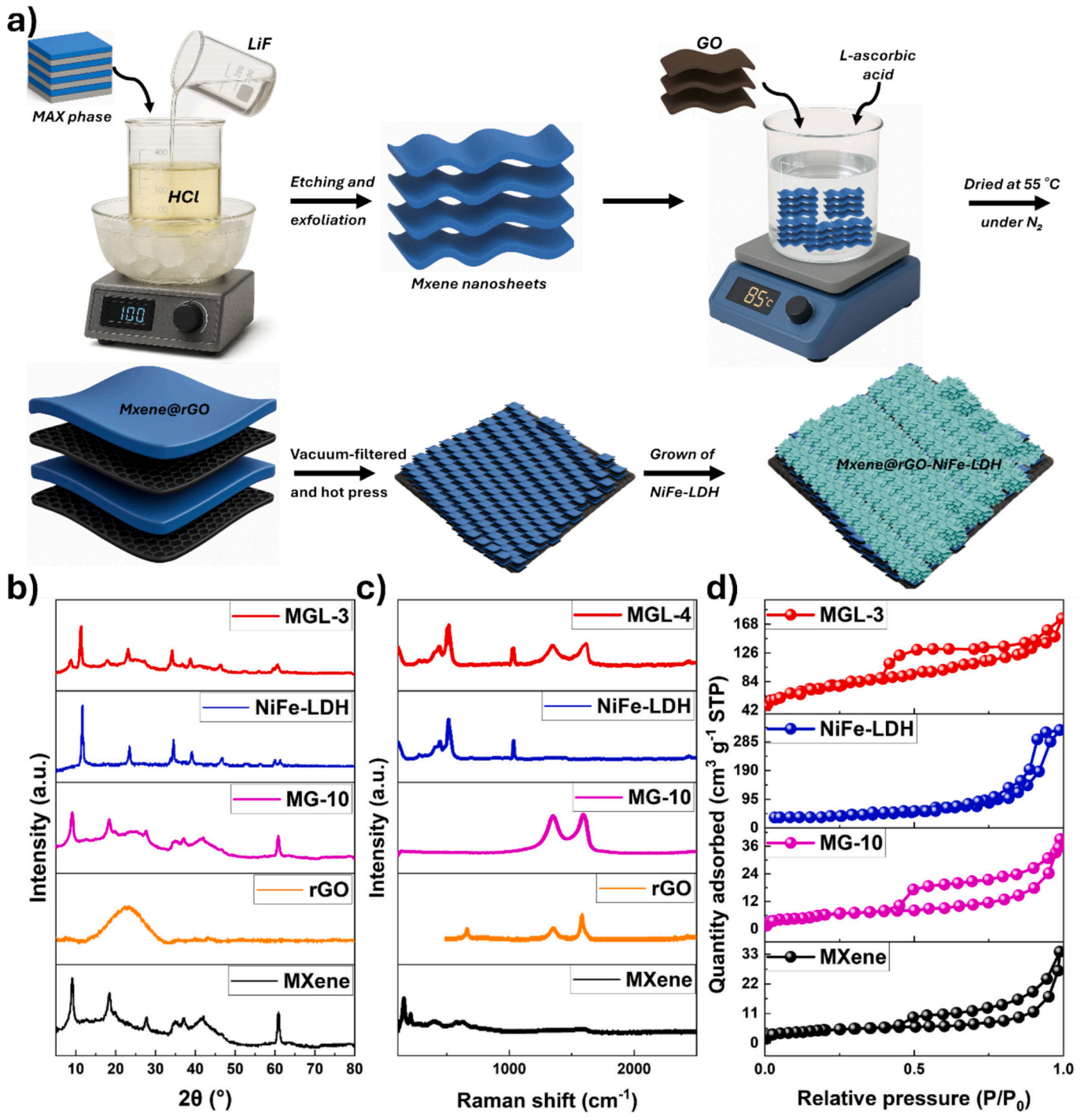

Fig. 1. (a) Schematic illustration of the synthesized procedure of the MXene, MG, and MGL electrodes; (b) XRD patterns of the elements, (c) Raman spectra of the elements; (d) N_2 adsorption-desorption analysis of MXene, MG-10, NiFe-LDH, and MGL-3.

2.5. Electrodeposition of NiFe-LDH nanosheets

NiFe-LDH was grown as the outer active layer by cathodic electrodeposition on the MXene@rGO/cloth films in nitrate electrolytes formulated to deliver Ni:Fe molar ratios of 4:1, 3:1, and 2:1. Deposition baths contained 0.050 M $Ni(NO_3)_2$ and $Fe(NO_3)_3$ at 0.0125 M (4:1), 0.0167 M (3:1), and 0.0250 M (2:1), with 1 mmol.L^{-1} $NaNO_3$ as supporting electrolyte. The MXene@rGO/cloth served as the working electrode in a three-electrode cell (Ag/AgCl reference, Pt counter). After a 5 min open-circuit pre-soak, deposition proceeded potentiostatically at −1.05 *V* vs Ag/AgCl for 360 s. Local nitrate reduction generated OH^- at the interface and drove in-situ precipitation of ultrathin NiFe-LDH nanosheets conformally anchored to the MXene@rGO scaffold. Electrodes were rinsed with water and ethanol and dried at 60 °C under N_2. For clarity, the final composites are denoted MGL-4 (Ni:Fe = 4:1), MGL-3 (Ni:Fe = 3:1), and MGL-2 (Ni:Fe = 2:1). The schematic diagram of the synthesized components is shown in Fig. 1a.

2.6. Characterization

Details of all characterization methods are provided in Text S2 of SI.

2.7. Electrochemical measurement

Details of electrochemical measurements are expressed in Text S3 of SI.

2.8. Electroadsorption experiments

Electroadsorption was conducted in custom acrylic unit cells (Fig. S1) under dark (shaded) conditions. The synthesized MG and MGL electrodes served as the anode, and the titanium plate was used as the cathode; the interelectrode gap was fixed at 5 mm. For kinetics, 40 mL of PFOA solution (10 mg L^{-1}) containing 1 mmol L^{-1} $NaNO_3$ at pH 6.00 ± 0.10 was polarized at +0.8 *V* (anode vs cathode), and aliquots were taken at defined times to track concentration decay. For capacity measurements (isotherms), initial PFOA concentrations of 0.5–10 mg L^{-1} were tested under identical conditions, with an equilibrium time of 16 h determined from kinetic experiments. Unless otherwise noted, all runs used freshly prepared working solutions (from methanolic PFOA stock), and were performed in at least triplicate. Removal efficiency, equilibrium, and time-dependent adsorption capacity were evaluated from the following Eq. [33]:

$$\text{Removal rate}\ (\%) = (1 - C_t/C_0) \times 100 \quad (1)$$

$$q_e = (C_0 - C_e) \times V/m \quad (2)$$

$$q_t = (C_0 - C_t) \times V/m \quad (3)$$

where C_0, C_e, and C_t are the initial, equilibrium, and time-(t) concentrations, V is solution volume, and m is the mass of active material. In calculating adsorption capacity, the electrode mass corresponds to the mass of the active material deposited on the carbon cloth (MXene@rGO scaffold plus NiFe-LDH). In other words, the mass of the carbon cloth current collector was excluded because it functions only as a conductive support and would otherwise dilute the capacity values.

To evaluate desorption and reusability, tests were performed at C_0 = 1 mg L^{-1} PFOA. After reaching electroadsorption equilibrium, half of the solution volume was replaced with one of three desorption electrolytes: 1 mmol L^{-1} $NaNO_3$, ethanol, or a 1:1 (v/v) ethanol/1 mmol L^{-1} $NaNO_3$ mixture. The electrode polarity was then reversed (−0.8 V) for desorption. All other conditions matched the adsorption step. This capture–release operation was repeated five cycles. Moreover, parameter studies were evaluated at C_0 = 1 mg L^{-1} PFOA by varying pH 4–10 (1 mM $NaNO_3$; adjusted with dilute HNO_3/NaOH), ionic strength 0–10 mM $NaNO_3$ at pH 6.00, assist voltage 0 − +1.2 V (anode positive), and humic acid 0–10 mg L^{-1}. Furthermore, details of electroadsorption kinetics and isotherm modeling are provided in Text S4 of SI.

2.9. Analytical method

PFOA concentrations were quantified by ultra-performance liquid chromatography (UPLC). Full analytical details are provided in Text S5 of SI.

3. Results and discussion

3.1. Characterization of the synthesized electrodes

Fig. 1b shows the X-ray diffraction (XRD) of MXene, rGO, MG-10, NiFe-LDH, and MGL-3, and Fig. S2b illustrates the XRD patterns of the MAX phase, MG-5, MG-15, MGL-2, and MGL-4. Fig. S2b shows the Ti_3AlC_2 MAX phase indexed to the standard pattern, with a sharp peak at 38.8° (1 0 4) from the Al-containing layer. In Fig. 1b, this 38.8° peak disappeared after etching, confirming removal of Al and transformation to $Ti_3C_2T_x$ MXene [34]. Moreover, the MXene pattern then displayed features at ~18.4° (assigned to (0 0 6) of $Ti_3C_2F_2$), 27.4° (attributed to $Ti_3C_2(OH)_2$), and 60.8° (assigned to (1 1 0) of Ti_3C_2). These peaks indicated —F and —OH surface terminations on the MXene [35]. Compared with MAX, the broader MXene peaks indicate higher structural disorder and exfoliation consistent with conversion from a 3D carbide to a layered material [36].

Furthermore, in Fig. 1b, rGO shows a broad (0 0 2) ~23.3° [37]. For MG-10 (and MG-5/MG-15 in Fig. S2a), the MXene peaks were retained but slightly broadened while the rGO (0 0 2) became more diffuse, consistent with intimate mixing and reduced MXene restacking [38]. The NiFe-LDH reference in Fig. 1b exhibited the expected series 11.6° (0 0 3), 23.4° (0 0 6), 34.5° (0 1 2), 39.2° (0 1 5), 46.6° (0 1 8), 59.8° (1 1 0), 60.8° (1 1 3) (PDF#40-0215) [39]. These LDH peaks appear in MGL-3 (Fig. 1b) and in MGL-2/MGL-4 (Fig. S2a), confirming LDH deposition on MXene@rGO. Based on Fig. 1b, the $Ti_3C_2T_x$ (0 0 2) peak of the composite shifts to lower 2θ compared with pristine MXene, indicating a larger interlayer spacing (consistent with rGO spacing and anchored LDH nanosheets) [40].

The Raman spectra of the MGL composites and the individual constituents are presented in Fig. 1c and Fig. S2b, respectively.

Based on Fig. 1c, pristine $Ti_3C_2T_x$ showed an A_{1g} mode near 200 cm^{-1} attributed to Ti vibrations. E_g modes appeared at 398 and 621 cm^{-1}, arising from in-plane Ti—C motions with contributions from surface terminations (—F, —OH, —O) [41]. Moreover, rGO illustrated the carbon D and G bands at 1350 and 1590 cm^{-1}, respectively, with a weak, broadened 2D overtone in the 2650–2720 cm^{-1} region (Fig. 1c) [42]. Upon combining MXene with rGO, the MXene E_g features remain discernible but shift to higher wavenumbers and broaden slightly, indicating perturbation of the Ti—C lattice and its surface terminations by interfacial coupling. Concomitantly, the G band of rGO upshifted relative to 1590 cm^{-1}, consistent with charge transfer and strain imposed by intimate MXene–graphitic contact [43]. These interfacial effects were reflected quantitatively in the D-to-G intensity ratio. Using the reference values rGO I_D/I_G = 0.48, MG-5 (95:5), MG-10 (90:10), and MG-15 (85:15) exhibited I_D/I_G = 0.90, 0.96, and 0.94, respectively. The substantial increase from 0.49 to 0.90–0.96 demonstrated defect activation and domain fragmentation in rGO induced by MXene anchoring [44]. The maximum I_D/I_G at MG-10 indicated the strongest interfacial distortion and electronic interaction without excessive MXene coverage. At higher MXene loading (MG-15), the slight decrease in I_D/I_G was consistent with partial masking of rGO defects by MXene restacking or coverage. Thus, the preservation and mild hardening of MXene modes, the G-band upshift, and the I_D/I_G evolution identify MG-10 as the optimal composition in the MXene@rGO series.

Moreover, the MGL electrodes (MGL-4, MGL-3, MGL-2; Fig. 1c and Fig. S2b) display a superposition of the three constituents with clear interfacial signatures. The $Ti_3C_2T_x$ lattice retains the A_{1g} and E_g features, which appear slightly upshifted relative to pristine MXene, consistent with perturbation of Ti—C bonding and termination fields at MXene–carbon/LDH interfaces [45]. The NiFe-LDH contributes metal–oxygen vibrations as bands near 445–525 cm^{-1}, which are also present in the pure LDH spectrum and confirm the hydroxide phase within the composite [46]. The graphitic framework shows the rGO D and G bands, with the G band shifted to higher wavenumber than pristine rGO, consistent with interfacial charge transfer/strain [47]. Among the series, MGL-3 (Ni:Fe = 3:1) combines the moderate $I_D/I_G \approx 0.94$ with the sharpest LDH signatures and well-defined MXene modes, indicating the best balance between interfacial interaction and structural order under identical measurement conditions.

Figs. 1d and S2c show the N_2 sorption isotherms and BET surface areas of the samples. MGL-3 exhibited a *meso*−/macroporous texture with a BET surface area of 255.4 $m^2\ g^{-1}$, which is about 2.18 times that of NiFe-LDH (117.2 $m^2\ g^{-1}$) and about 14.6 times that of $Ti_3C_2T_x$ MXene (17.5 $m^2\ g^{-1}$). The MG scaffolds alone remain low in area (MG-5: 22.4, MG-10: 28.7, MG-15: 24.1 $m^2\ g^{-1}$), indicating only modest mitigation of MXene restacking by rGO. LDH decoration markedly increased porosity: MGL-2 and MGL-4 reach 237.2 and 242.1 $m^2\ g^{-1}$, respectively, but both

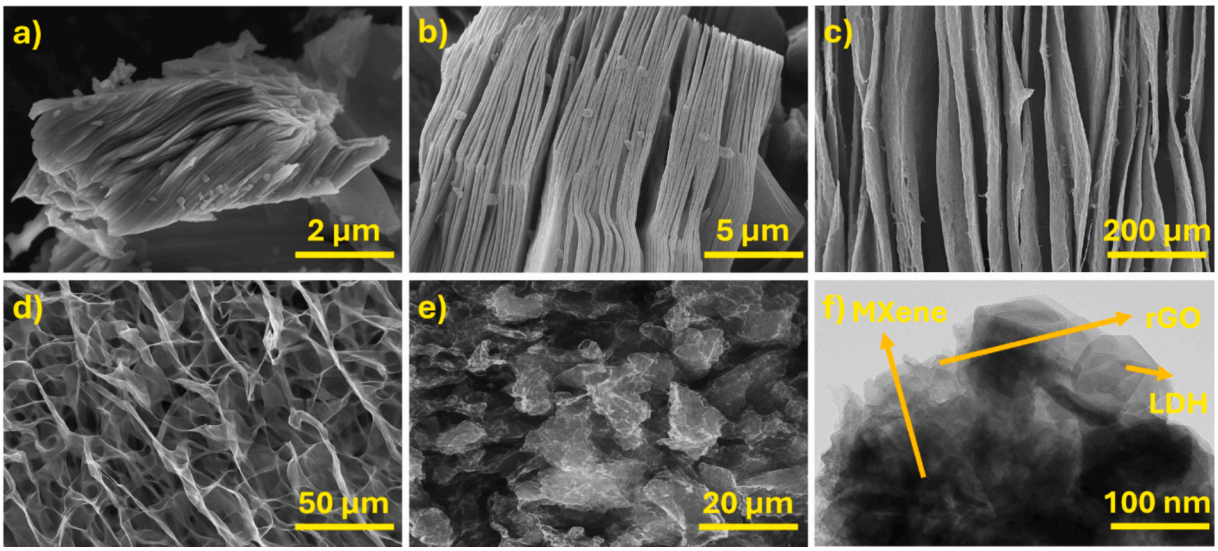

Fig. 2. SEM image of the (a) MAX phase; (b) MXene; (c) crosse sectional view of MG-10; (d) MG-10; (e) MGL-3; and (f) TEM image of the MGL-3.

remain below MGL-3. This shows that the MGL-3 provided the highest surface area and the most favorable porous architecture among all samples. While BET surface area reflects the textural accessibility of the porous framework, the electrochemically active surface area (ECSA) can differ from BET and would require dedicated electrochemical quantification, which is outside the scope of the present work.

Fig. 2a shows the scanning electron microscopy (SEM) figure of Ti_3AlC_2 MAX phase as compact, smooth lamellae with tightly bonded layers. The SEM of $Ti_3C_2T_x$ MXene with an accordion-like morphology of separated sheets and open galleries, evidencing Al removal and partial delamination, is illustrated in Fig. 2b. Moreover, Fig. 2c depicts the SEM image of MG-10 in cross-section, revealing vertically stacked, delaminated lamellae with open slit-like channels across the film thickness. The SEM image of MG-10 from the surface, illustrating a wrinkled, interconnected sheet network that forms an open porous scaffold, is shown in Fig. 2d. Furthermore, Fig. S3a shows the SEM image of NiFe-LDH, revealing cauliflower-like aggregates composed of plate-like crystallites that coalesce into micron-scale secondary particles.

The SEM image of MGL-3 (Fig. 2e) revealed a crumpled, lamellar MXene@rGO framework that uniformly decorated with NiFe-LDH nanosheets. The roughened sheet surfaces, inter-sheet bridges, and abundant interstitial voids indicate a hierarchical porous network in which LDH coats and links the MXene@rGO layers. For further observation, the transmission electron microscopy (TEM) image of MGL-3 is depicted in Fig. 2f. This figure shows overlapping nanosheets with clear depiction of each element in the final composite.

Additionally, Fig. S3b shows the cross-sectional EDS elemental maps of MGL-3. The Ni and Fe elements were uniformly distributed and co-localized with O, confirming a continuous NiFe-LDH coating through the film thickness, while C and Ti map the underlying MG scaffold. No isolated Ni/Fe-rich agglomerates or composition gradients are evident, indicating homogeneous integration of LDH with the lamellar framework.

3.2. Electrochemical properties

Cyclic voltammetry (CV) was employed to benchmark the electrodes, noting that larger integrated CV area generally reflects higher specific capacitance. As shown in Fig. 3a–d, MXene, MG-10, and MGL-3 exhibit stable, quasi-rectangular envelopes without discernible redox peaks, consistent with predominantly electric double-layer (EDL) storage [48]. Among them, MGL-3 encloses the largest area, translating to the highest capacitance, outperforming MG-10 and MXene, based on Fig. 3a. The improvement is attributed to the composite architecture, including rGO spacing and NiFe-LDH nanosheets, which provides continuous electron pathways and abundant accessible interfaces, thereby facilitating charge accumulation. Moreover, as the scan rate increases, the specific capacitance of all electrodes declines, reflecting limited ion penetration into inner pores at short timescales. Notably, MGL-3 retains a clear lead at all scan rates, underscoring its superior and robust charge-storage performance. Moreover, galvanostatic charge–discharge (GCD) tests are shown in Fig. 3e and f. At 1 A g^{-1} (Fig. 3e), MGL-3 exhibits the longest discharge time, corroborating its superior charge-storage and release behavior. The calculated specific capacitances confirm this trend: MGL-3 = 266 F g^{-1}, versus MG-10 = 159 F g^{-1} and MXene = 115 F g^{-1}. As the current varies (Fig. 3f), the capacitances of all three electrodes decrease, yet MGL-3 maintains a clear advantage across the entire current range, in full agreement with the CV results.

Furthermore, Fig. 3g illustrates the electrochemical impedance spectroscopy (EIS) of the MXene, MG-10, and MGL-3 electrodes. EIS was used to probe electronic/ionic transport in the three electrodes. In the Nyquist plots, the high-frequency intercept gives the solution/interfacial resistance (R_s). In this plot, the semicircle diameter reflects charge-transfer/pseudocapacitive resistance [49], and the low-frequency inclined line relates to ion diffusion toward the electrode [50]. Fitting the equivalent circuit (Fig. 3g) yields R_s = 1.79 Ω (MXene), 1.21 Ω (MG-10), and 0.78 Ω (MGL-3); correspondingly. Thus, MGL-3 shows the smallest arc and the steepest low-frequency slope, indicating the most efficient electron pathways and facilitated ion transport, consistent with its CV/GCD superiority.

To elucidate the charge-storage kinetics of the MGL-3 electrode, CV was recorded at scan rates of 0.2–1.0 mV s^{-1} (Fig. 3h). The peak current i scales with scan rate v according to the following Eq. [51]:

$$i = av^b \tag{4}$$

This equation can be linearized as follows:

$$\log(i) = \log(a) + b\log(\upsilon) \tag{5}$$

In Eq. (5), $b \approx 1$indicates surface-controlled (capacitive) processes, whereas $b \approx 0.5$ signals diffusion-limited behavior. The extracted b-values fall in the range 0.80–0.95 (Fig. S4), indicating that charge storage in MGL-3 is predominantly surface-controlled (capacitive) with a measurable diffusion contribution. To further separate contributions at a given potential V, the current was deconvoluted via Dunn's method as follows [52]:

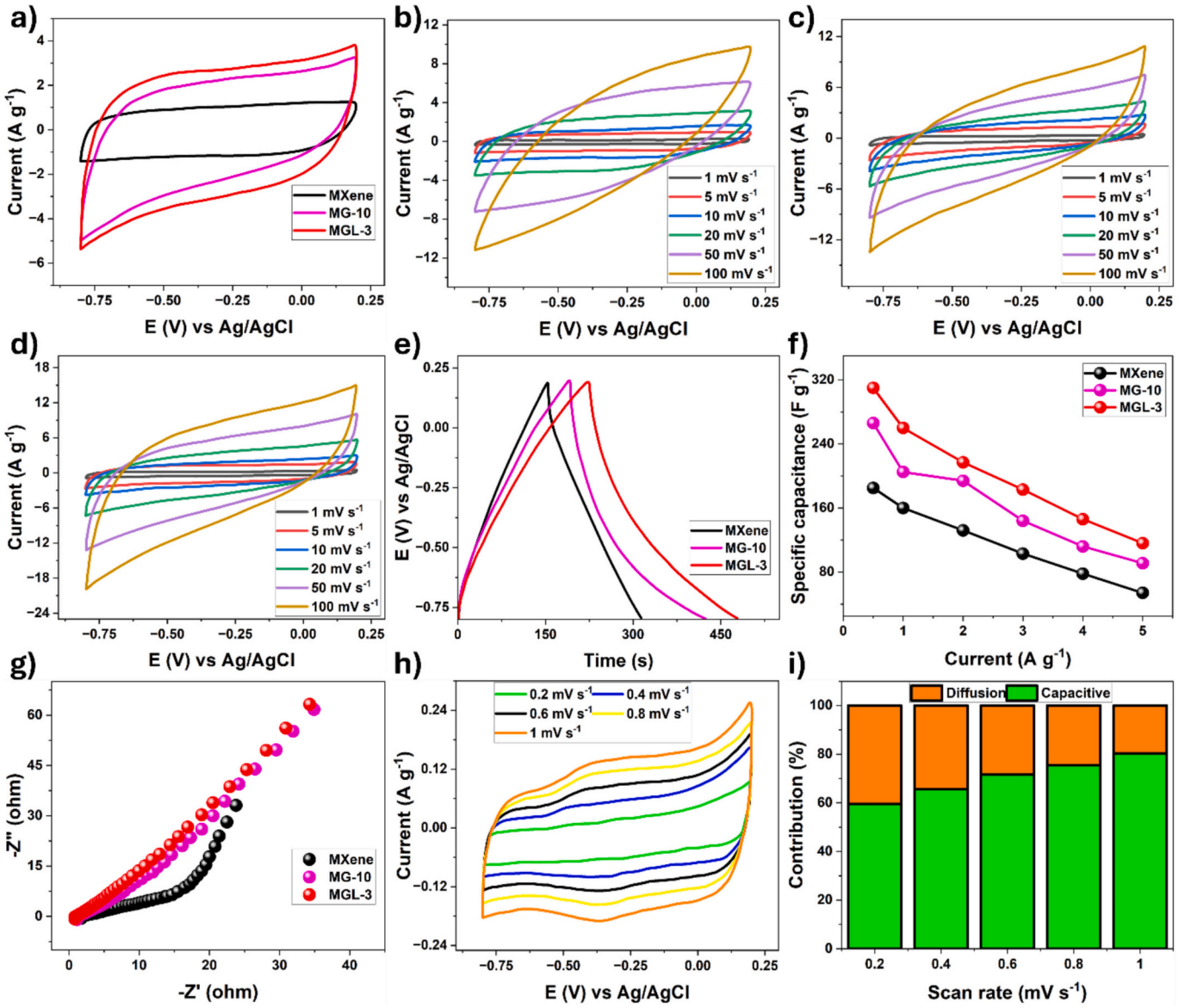

Fig. 3. (a) CV curves of MXene, MG-10, and MGL-3 at 5 mV s^{-1}; (b-d) CV curves of MXene, MG-10, and MGL-3 at different scan rates (e) GCD curves; (f) the specific capacitances at various current; (g) the Nyquist plots; (h) CV curves of the MGL-3 electrode at scan rates of 0.2–1.0 mV s^{-1}; and (i) Fractional contributions of capacitive and diffusion-controlled processes to the total current at each scan rate.

$$i = k_1 \upsilon + k_2 \upsilon^{1/2} \quad (6)$$

where $k_1 v$represents the capacitive term and $k_2 v^{1/2}$ the diffusion-controlled term. The capacitive fraction at each v was then evaluated as $k_1 v/i(V)$, enabling a quantitative comparison of kinetics across scan rates. Capacitive-controlled behavior reflects a rapid, surface-governed process, whereas diffusion-controlled behavior corresponds to slower kinetics limited by solid-state diffusion and mass transfer. A larger capacitive fraction indicates a greater density of accessible active sites and faster, more reversible ion adsorption/intercalation. Consequently, electrodes with higher capacitive contributions deliver superior rate performance.

Additionally, as the scan rate rises from 0.2 to 1.0 mV s^{-1}, the capacitive contribution increases from 59.6% to 80.4% (Fig. 3i), indicating a growing dominance of fast surface processes. This high capacitive fraction stems from the properties of MGL-3, where rGO prevents aggregation of MXene and NiFe-LDH, exposes more active sites, and provides a conductive bridge that accelerates charge transfer. The orderly dispersion of MXene and NiFe-LDH creates continuous, accessible ion pathways, enabling rapid ion storage kinetics across the electrode.

3.3. *Effect of pH values of electrolyte*

Fig. 4a compares PFOA removal by MGL-3 under close and at open circuit from pH 4 to 10. When the circuit is closed, removal efficiency decreases from 98.45% (pH 4) to 86.39% (pH 10). However, when the circuit is opened, it falls more sharply from 80.51% to 49.35%. Because the initial and equilibrium pH values were essentially unchanged (Table S1), these trends arise from interfacial charge effects rather than pH drift during testing. Given the pK_a of PFOA ≈ − 0.5, PFOA remains fully anionic across this range [53]. At mildly acidic pH, the MGL-3 surface is more protonated/positively charged, strengthening electrostatic attraction and interlayer anion exchange, which was further shown by the pH of zero point of charge in Fig. S5. As pH increases toward 10, deprotonation of hydroxide layers and MXene terminations reduces net positive charge and increases competition from OH^-/NO_3^-, so removal declines. Nevertheless, the applied field sustains

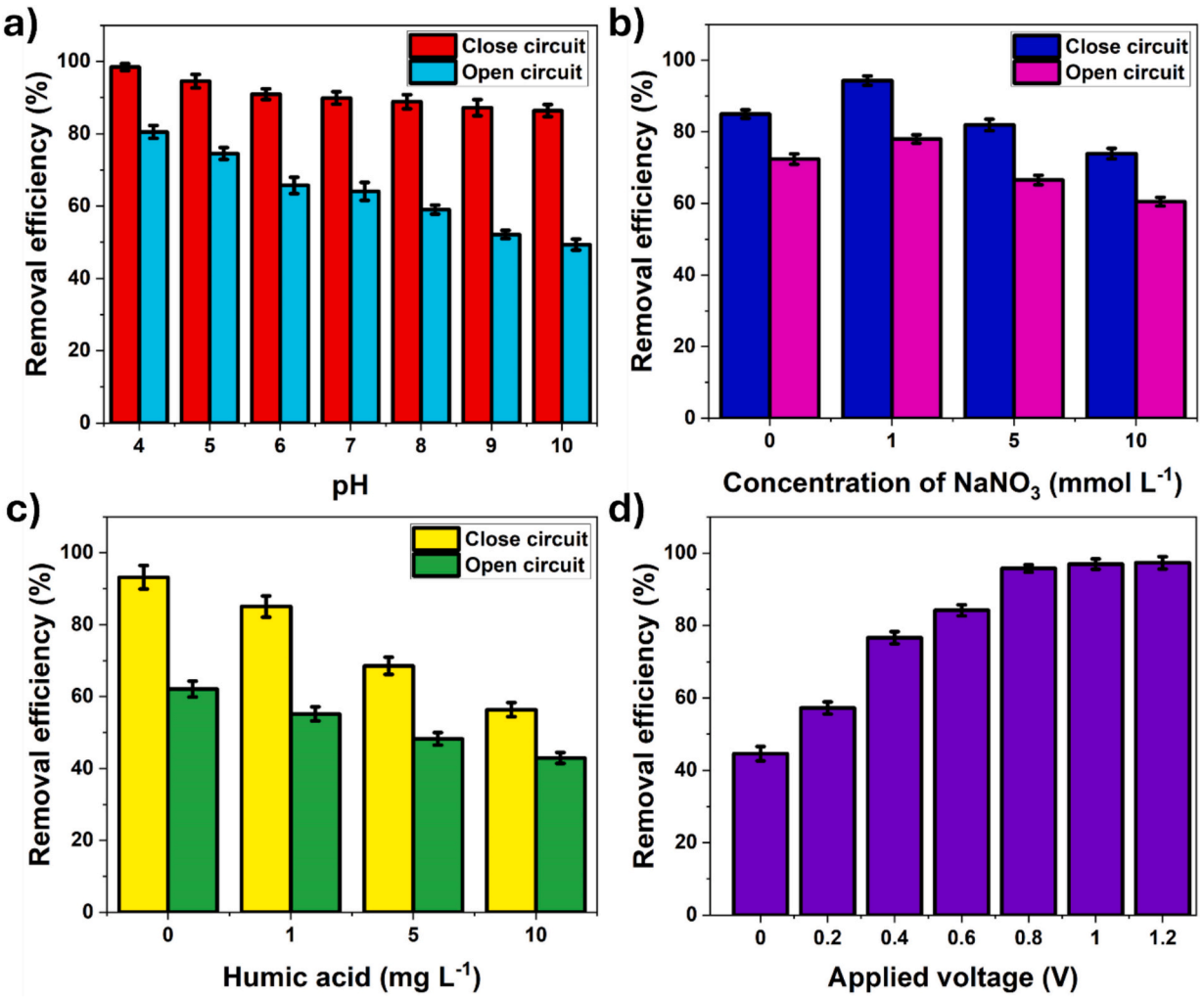

Fig. 4. Removal efficiency of PFOA through electroadsorption by MGL-3 (a) effect of pH; (b) effect of $NaNO_3$ concentration; (c) effect of humic acid; and (d) effect of applied voltage.

substantially higher uptake than open circuit, underscoring the robustness of electroadsorption and its preference for mildly acidic to near-neutral conditions [54].

3.4. Effect of ionic strength of electrolyte

Fig. 4b shows PFOA removal by MGL-3 as a function of $NaNO_3$ concentration under close and open-circuit conditions. For MGL-3, PFOA removal exhibits a maximum at 1 mM $NaNO_3$. Under closed condition, the removal efficiency is 94.33% at 1 mM, compared with 84.96% (0 mM), 81.93% (5 mM), and 73.93% (10 mM). At open circuit, the same optimum appears: 78.02% (1 mM) versus 72.38%, 66.53%, and 60.49% at 0, 5, and 10 mM, respectively. The improvement from 0 to 1 mM is attributed to better solution conductivity and reduced ohmic loss, which allow the electrode to operate closer to the applied potential and facilitate charge accumulation. The decline at higher salinity reflects compression of the electric double layer and increasing co-ion (NO_3^-) competition for positively charged LDH sites [55]. Moreover, partial Na^+–$PFOA^-$ pairing may further diminish the effective charge of the target anion. Across all ionic strengths, the closed condition exceeds open-circuit performance, confirming a robust electroadsorptive enhancement. Overall, 1 mM $NaNO_3$ provides the most favorable balance between conductivity and interfacial competition for the MGL-3 electrode. Moreover, the influence of common anions (Cl^- and SO_4^{2-}) and ionic strength (0 to 10 mM) on PFOA electrosorption capacity is summarized in Fig. S6.

3.5. Effect of humic acid

Fig. 4c shows the effect of humic acid (HA) on PFOA removal by MGL-3 under closed and open-circuit conditions. Under close circuit, removal efficiency declines monotonically from 93.21% (0 mg L^{-1} HA) to 56.38% (10 mg L^{-1}). Moreover, at open circuit, removal efficiency decreases from 62.13% to 42.93%. These trends are consistent with the known behavior of natural organic matter. Firstly, HA is predominantly anionic at near-neutral pH and competes with $PFOA^-$ for the positively charged LDH sites [56]. Secondly, HA adsorbs on the electrode, partially blocking pores and active edges (surface fouling). Finally, HA can associate with perfluoroalkyl chains in solution, lowering the activity of freely available $PFOA^-$ near the interface [57]. The applied potential still confers a substantial advantage versus open circuit, but its benefit diminishes as HA increases, indicating that electrostatic attraction cannot fully offset competitive adsorption and fouling at high NOM levels. Thus, MGL-3 remains effective under close circuit, even at 10 mg L^{-1} HA it removes 56% of the PFOA. However, the results highlight the importance of minimizing NOM or employing regeneration/pretreatment when treating humic-rich waters.

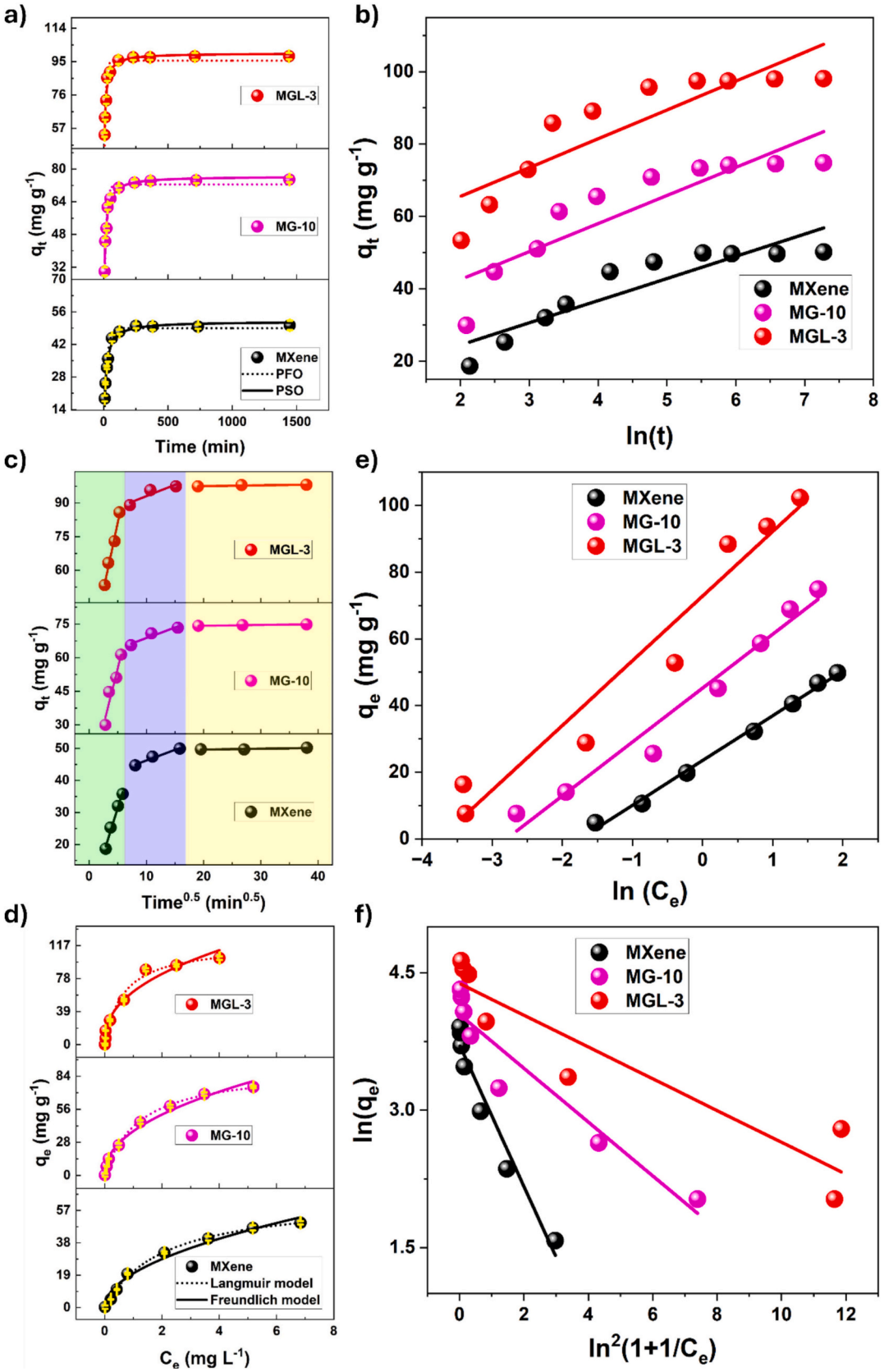

Fig. 5. (a) PFO and PSO models; (b) Elovich kinetic model; (c) Intra-particle diffusion model; (d) Langmuir and Freundlich electroadsorption isotherms; (e) Temkin isotherm; and (f) D–R isotherm for PFOA on MXene, MG-10, and MGL-3 at 25 °C (1 mM $NaNO_3$, pH 6.00 ± 0.10, +0.8 *V*).

Table 1
Comparison of reported PFOA adsorption/electroadsorption capacities and conditions for representative adsorbents.

Adsorbent	Types of adsorptions	PFOA concentration	Applied voltage	pH range	Adsorption rate constant (g/mg·min)	Regeneration	Q^{o}_{max} (mg g^{-1})	Reference
MXene-PEDOT:PSS (poly(3,4-ethylene dioxythiophene) polystyrenesulfonate)	Electroadsorption	750 ppb	+1 V	–	1.4×10^{-4}	5 cycles at −1 V	51.10	[65]
Copper oxide-modified multi-walled carbon nanotubes (CuO-CNTs)	Electroadsorption	100 to 8000 μg L^{-1}	0.6 V	3 to 9	0.2 (mg/μg·h)	4 cycles at −0.6, −1, and − 1.5 V	231.67	[69]
MGL-3	Electroadsorption	0.5 to10 mg L^{-1}	+0.8 V	4 to 10	0.0016	10 cycles at −0.8 V	119.52	This study
MG-10	Electroadsorption			4 to 10	0.0014	–	91.59	
MIL-96(Al)	Adsorption	1 to 100 mg L^{-1}	–	3 to 11	0.035	4 cycles	71.4	[70]
Magnetic chitosan biopolymeric spheres	Adsorption	10 to 50 mg L^{-1}	–	3 to 10	0.0137	5 cycles	16	[71]

3.6. Effect of applied voltage

Fig. 4d illustrates that raising the applied potential steadily increases PFOA removal on MGL-3 from 44.60% (0 V) to 95.78% (0.8 V). However, the removal efficiency increases slightly at higher applied voltage and changes from 96.99% at 1.0 V to 97.34% at 1.2 V. Up to +0.8 V, removal increases sharply. The higher field accelerates migration of $PFOA^{-}$ to the positively biased surface and compacts the electric double layer. The resulting larger current strengthens electrostatic attraction at the MXene@rGO–LDH interface. Beyond +0.8 V, the removal curve approaches a plateau. This indicates that available adsorption sites and near-surface PFOA concentration become limiting (site saturation and transport constraints). Additional voltage offers little benefit but increases energy consumption and the risk of parasitic reactions [58]. Thus, +0.8 V is an efficient operating point, delivering >95% removal and within ~1.6% points of the maximum observed value.

3.7. Electroadsorption kinetics

The electroadsorption kinetics of PFOA on MGL-3 were analyzed with the pseudo–first-order (PFO) and pseudo–second-order (PSO) models, as shown in Fig. 5a. The uptake is rapid during the first 40 min, followed by a slower approach to equilibrium at about 150 min. The fast stage reflects field-driven accumulation of $PFOA^{-}$ at the positively biased MGL surface and abundant accessible sites. Moreover, the subsequent slowdown arises from progressive site filling and slower diffusion into internal lamellae and pores [59].

The fitting parameters for all kinetic models are summarized in Table S2. For MGL-3, the PSO model provides the higher coefficient of determination ($R^2 = 0.987$ for PSO and 0.941 for PFO) and an equilibrium capacity. PSO's superior fit reflects the coexistence of physisorption and chemisorption under bias, consistent with the observed rapid initial uptake followed by a more gradual approach to equilibrium [60]. Furthermore, comparing electrodes, MGL-3 shows the highest electroadsorption capacity of 99.78 mg g-1, followed by 76.43 for MG-10 and 51.88 mg g^{-1} for MXene. The PSO initial rate (υ_0) increases from 3.50 (MXene) to 8.18 for MG-10 and to 15.93 mg g^{-1} min^{-1} for MGL-3, confirming progressively faster early-time uptake. Additionally, in the PFO model, K_1 (min^{-1}) is the apparent first-order rate constant governing how quickly uptake approaches equilibrium. As presented in Table S2, K_1 increases from 0.0449 (MXene) to 0.0637 for MG-10 and to 0.0915 min^{-1} for MGL-3.

Furthermore, based on Fig. 5b, Elovich model highlights that MGL-3 possesses the most active and heterogeneous surface among the three electrodes [61]. Based on Table S2, the initial rates (α) of 44.96 (MXene), 254.16 (MG-10), and 4010.12 mg g^{-1} min^{-1} (MGL-3), showing a dramatic rise in early-time uptake. The desorption/heterogeneity parameter (β) is 0.163 (MXene), 0.129 (MG-10), and 0.125 g mg^{-1} (MGL-3), indicating a slower decline of rate with surface coverage and greater heterogeneity in the composites.

Adsorption generally proceeds through three sequential regimes: (1) rapid transport across the liquid boundary layer (film diffusion), (2) diffusion through accessible pores/paths within the electrode network (intraparticle diffusion), and (3) a final stage where uptake slows as active sites approach saturation and equilibrium [62]. Consistent with this mechanism, the Weber–Morris plots (q_t vs $t^{1/2}$) can be divided into three linear segments for all electrodes (Fig. 5c), indicating that the overall adsorption kinetics are governed by multiple steps rather than a single diffusion process. Notably, none of the fitted lines passes through the origin ($C \neq 0$), confirming that intraparticle diffusion contributes to adsorption but is not the sole rate-limiting step, and that boundary-layer resistance is also significant [63].

In this model, the slope K_i (mg g^{-1} $min^{-1/2}$) reflects the apparent uptake/transport rate in each regime, while the intercept C (mg g^{-1}) is associated with the boundary-layer effect. Larger C values indicate a greater contribution from external mass-transfer resistance and/or stronger initial surface uptake. As summarized in Table S2, the rate constants follow $K_{i1} > K_{i2} > K_{i3}$ for all samples, consistent with fast initial adsorption followed by slower diffusion and eventual site saturation. Moreover, MGL-3 exhibits higher K_{i1} (12.04) and K_{i2} (1.01) than MG-10 ($K_{i1} = 10.28$; $K_{i2} = 0.94$) and MXene ($K_{i1} = 5.74$; $K_{i2} = 0.66$), demonstrating faster film transfer and intraparticle diffusion in the composite electrode. Meanwhile, the intercepts increase across the three stages ($C_1 < C_2 < C_3$) and are overall larger for MGL-3 ($C_1 = 21.14$; $C_2 = 82.97$; $C_3 = 96.85$ mg g^{-1}), indicating a pronounced boundary-layer/surface uptake contribution during adsorption. Finally, the very small K_{i3} values (0.02 to 0.05) confirm the slow approach to equilibrium as adsorption sites become progressively saturated.

To rigorously quantify the electrosorption advantage relative to a defined passive baseline, a three-electrode control experiment was performed. In this test, the working electrode potential was held at 0 V vs Ag/AgCl and compared directly with +0.8 V vs Ag/AgCl, as shown in Fig. S7. The biased condition yields consistently higher uptake throughout the adsorption period. Moreover, the PSO fitting further shows that the applied potential accelerates early-time uptake, with the initial rate v_0 increasing from 8.22 to 17.11 mg g^{-1} min^{-1}. These results confirm that the electric field provides a measurable enhancement in both adsorption kinetics and equilibrium capacity beyond passive adsorption at fixed potential.

3.8. Electroadsorption isotherms

Isotherm analysis quantifies how equilibrium uptake varies with concentration and reveals surface capacity, affinity, and heterogeneity. In this study, PFOA isotherms were fitted with Langmuir, Freundlich, Temkin, and Dubinin–Radushkevich (D–R) models, as plotted in

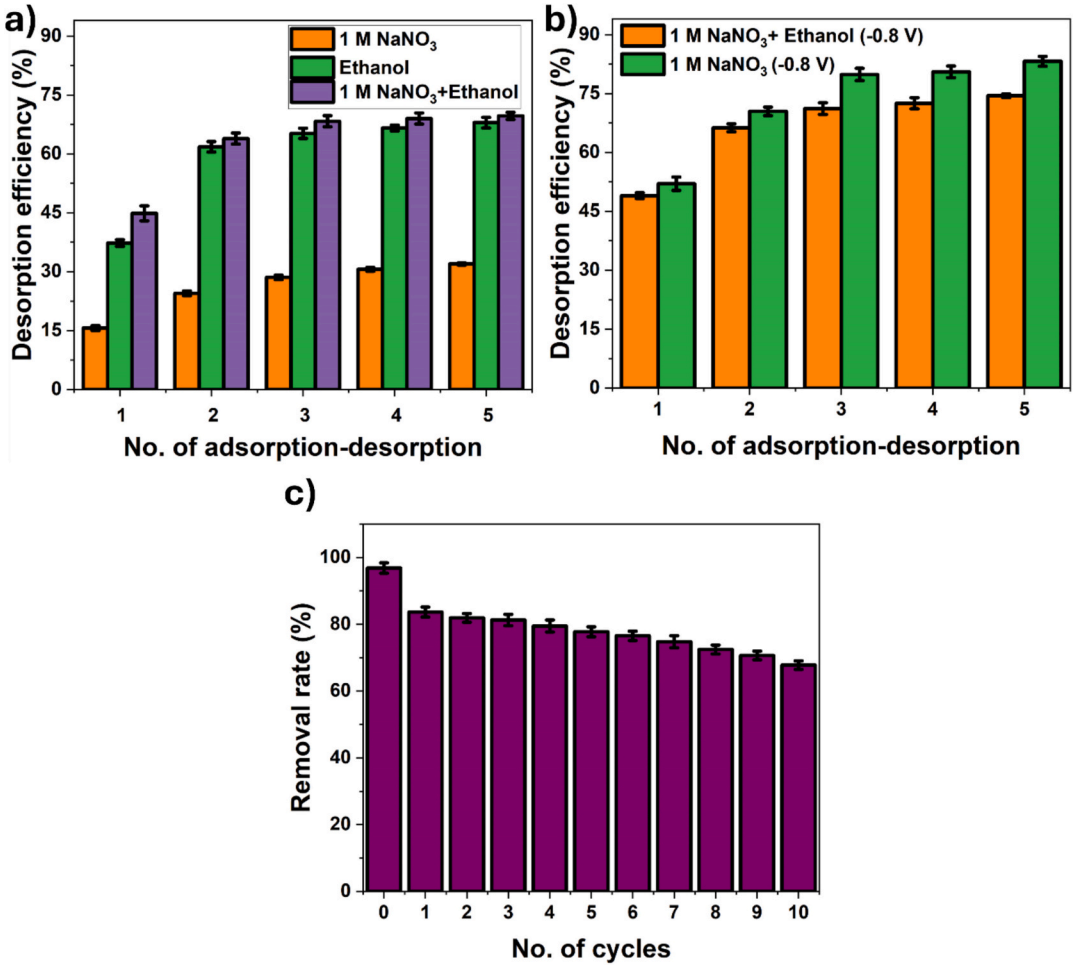

Fig. 6. Regeneration performance of the MGL-3 electrode for PFOA removal: (a) Desorption efficiency (%) vs cycle number for 1 mM $NaNO_3$, ethanol, and ethanol/$NaNO_3$ under open-circuit conditions; (b) Desorption efficiency (%) vs cycle number under reverse bias (−0.8 V) using 1 mM $NaNO_3$ and ethanol/$NaNO_3$ as desorption electrolytes; (c) Cycling performance shown as adsorption removal efficiency (%) over 10 consecutive capture–release cycles.

Fig. 5d–f. The corresponding fit parameters and diagnostics are summarized in Table S3.

Fig. 5d shows Langmuir and Freundlich models for MXene, MG-10, and MGL-3. The Langmuir model provides the better description of the experimental data (higher R^2), indicating predominantly monolayer adsorption on a finite set of sites [64]. The Langmuir capacities increase from 64.55 mg g^{-1} for MXene to 91.59 mg g^{-1} for MG-10 and to 119.52 mg g^{-1} for MGL-3. Relative to MXene, MGL-3 delivers an ~85% higher Q_{max} and is ~31% higher than MG-10. Table 1 compares the Q_{max} of the existing electroadsorption/adsorption processes in the literature.

Under comparable electroadsorption conditions, MGL-3 outperforms MXene–PEDOT:PSS [65] and conventional adsorbents such as MIL-96 (Al) and magnetic chitosan spheres. Although CuO-CNTs report a higher capacity, MGL-3 achieves strong performance at a modest bias and in a similar concentration window, reflecting the effectiveness of the MXene@rGO–LDH architecture.

The Langmuir affinity constant (k_L) increased from 0.4899 (MXene) to 1.5322 (MGL-3), indicating stronger binding and a higher density of effective adsorption sites in the hybrid [66]. MGL-3 has about three times the Langmuir affinity of MXene and about 1.9 times that of MG-10.

Freundlich fits are also satisfactory but consistently lower R^2 values, supporting some surface heterogeneity without displacing the Langmuir preference. The Freundlich constant (K_F) increases from 20.02 to 62.58 (mg g^{-1})(L mg^{-1})$^{1/n}$, which is about three times higher for MGL-3 than for MXene and about 1.7 times higher than for MG-10. The adsorption intensity (n) is 1.97, 2.17, and 2.40 for MXene, MG-10, and MGL-3, respectively. Moreover, $n > 1$ indicates favorable adsorption, and the gradual rise in n is consistent with stronger affinity and more favorable uptake on the composite electrode [66].

The adsorption data were also well described by the Temkin model (Fig. 5e). The model indicates that adsorbate–adsorbate interactions are present and that the heat of adsorption decreases with surface coverage, as the model assumes. The Temkin binding constant (k_T) increased from 5.76 L g^{-1} for MXene to 16.45 L g^{-1} for MG-10 and 42.79 L g^{-1} for MGL-3, evidencing progressively stronger binding among these adsorbents. Conversely, the b_T parameter decreased from 184.43 J mol^{-1} (MXene) to 127.85 J mol^{-1} (MGL-3), suggesting that the composite offers more accessible sites while the average interaction energy per site is lower [67]. Moreover, the D–R model (Fig. 5f) implies that simple pore-filling is not the dominant mechanism. The mean adsorption energy (E) remained below 8 kJ mol^{-1} for all materials, which is lower than typical ion-exchange chemisorption energies (8–16 kJ mol^{-1}), indicating that PFOA uptake is governed mainly by physical interactions (electrostatic and hydrophobic) rather than pure chemical ion exchange [68].

3.9. Electroadsorption-desorption and recycling of MGL-3 electrode

Fig. 6a and b compare PFOA desorption from MGL-3 using different regeneration electrolytes under open-circuit conditions and under reverse bias. Under open circuit (Fig. 6a), the desorption efficiency at cycle 5 is 31.97% in 1 mM $NaNO_3$, 67.96% in ethanol, and 69.69% in ethanol/$NaNO_3$, demonstrating that ethanol-based eluents release PFOA

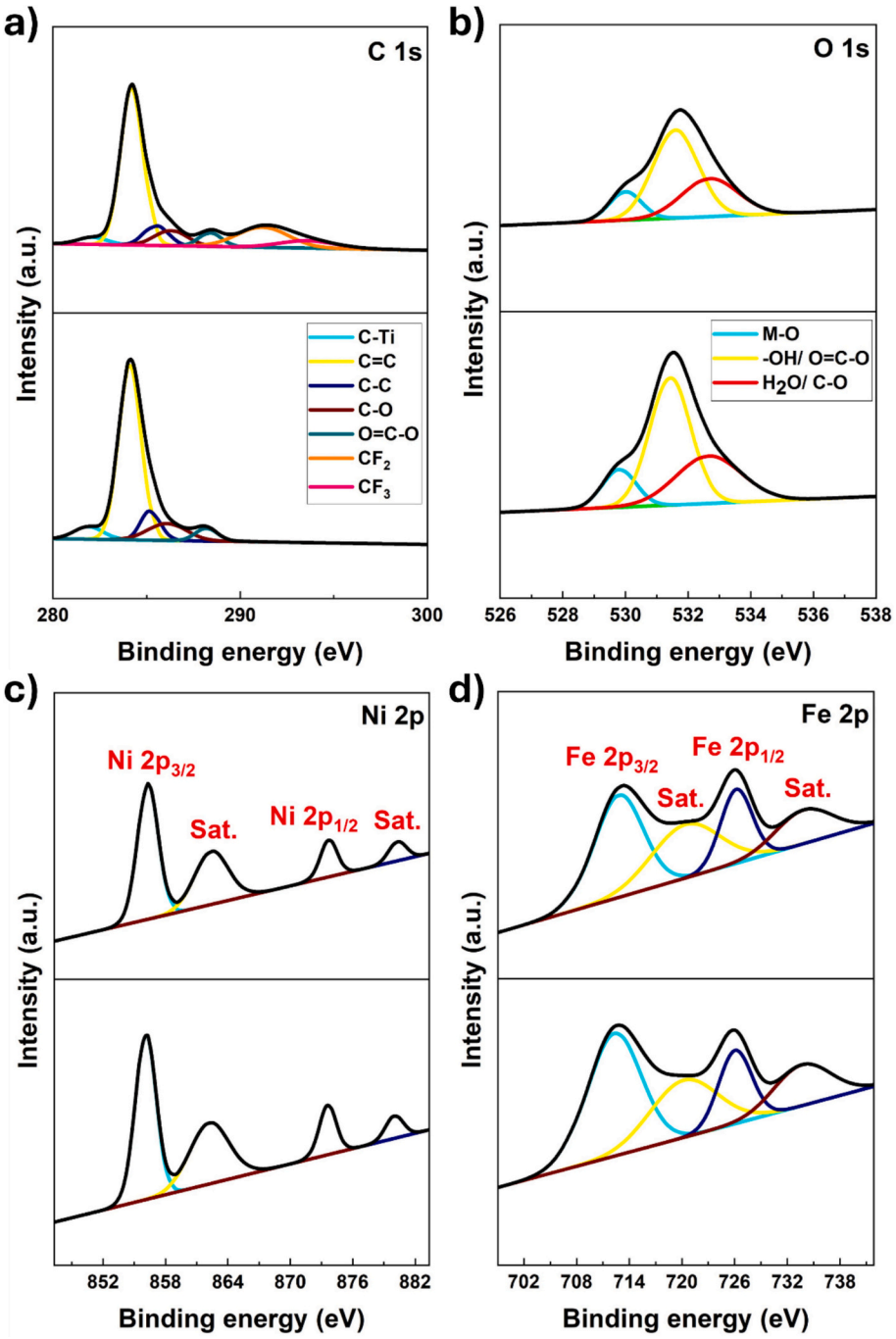

Fig. 7. XPS spectra of different elements before and after adsorption by PFOA through MGL-3 (a) C 1s; (b) O 1s; (c) Ni 2p; and (d) Fe 2p.

more effectively without applied voltage. Ethanol improves release over salt alone because it increases the solubility of PFOA and weakens hydrophobic association at the electrode surface [72]. Moreover, when a reverse bias was applied, the ethanol-containing desorption solution achieved a high release efficiency (74.47%, Fig. 6b), only slightly lower than that obtained with Na_2SO_4 (83.22%, Fig. 6b). This difference is likely linked to ethanol's properties as a polar organic solvent, which can reduce solution conductivity and hinder efficient electron/charge transport in the electrolyte [73]. Even at 83% desorption, ~17% remains on the electrode after regeneration, which can accumulate and reduce uptake over repeated cycles.

Multiple capture–release cycles were performed to assess the reusability of MGL-3 (Fig. 6c). The removal efficiency decreased from 96.83% (cycle 0) to 67.77% after 10 cycles. This gradual loss suggests regeneration is effective but not complete, likely due to residual strongly retained PFOA and/or progressive surface fouling that blocks some active sites [74]. Despite this decline, the electrode maintains substantial performance after repeated cycling, supporting practical reusability under the reverse-bias regeneration protocol.

SEM of the cycled MGL-3 in Fig. S8a shows the MGL remains intact and retains the lamellar MXene@rGO framework with LDH features still evident. However, the surface appears partially covered/compacted relative to the fresh electrode, suggesting progressive pore blocking or residual surface deposits after repeated regeneration. These morphological changes are consistent with the gradual performance loss over cycling, without indicating catastrophic structural failure [75]. Additionally, based on Fig. S8b, the XRD pattern after 10 electrochemical cycles shows only minor variations compared with the initial scan. The

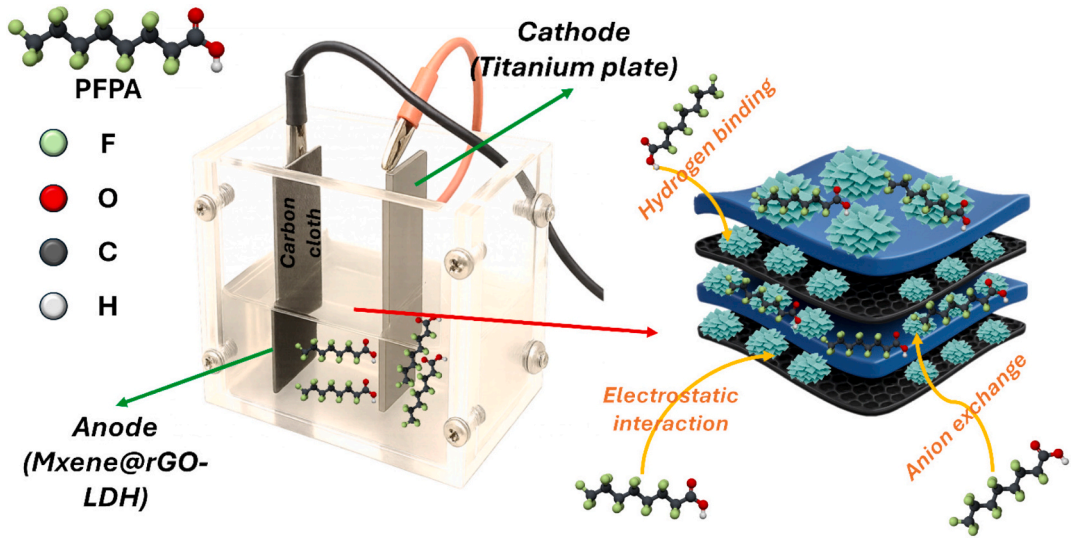

Fig. 8. Schematic illustration of the proposed electroadsorption of the PFOA on the MGL-3.

peak positions are largely retained, with at most a slight shift and subtle changes in relative intensity, indicating that the crystal structure remains mostly preserved during cycling. Thus, these small changes suggest good structural stability of the material after 10 cycles, with no evidence of major phase transformation or significant loss of crystallinity [76].

Moreover, Fig. S8c shows the XPS survey spectra of the MGL-3 electrode before and after 10 electroadsorption cycles. After cycling, the spectrum retains the characteristic signals of the electrode components (Ti, C, O, Ni, and Fe), indicating that no new elements are introduced and the composite framework remains present. Notably, the cycled electrode exhibits a more pronounced F signal together with an increased relative carbon contribution, while the metal-related signals (Ni/Fe/Ti) appear comparatively attenuated. This trend is consistent with the accumulation of a fluorocarbon-rich surface overlayer from residual PFOA-derived species that partially masks the underlying active surface, supporting the conclusion that the performance decay is primarily associated with transient surface fouling rather than bulk structural degradation.

3.10. Electroadsorption mechanism

X-ray photoelectron spectroscopy (XPS) probes the surface chemistry of MGL-3 with element- and bonding-level detail, letting us quantify adsorbed PFOA at the interface and see how adsorption perturbs local bonding. Fig. 7a presents the C 1s spectra of MGL-3 before and after PFOA electroadsorption. Before adsorption, the spectrum is deconvoluted into components at 281.9 eV (C—Ti), 284.1 eV (sp^2 C—C/C═C), 285.2 eV (sp^3 C—C/C—H), 286.1 eV (C—O), and 288.2 eV (O—C═O/carboxylate–carbonate), which are typical of the composite [77]. After adsorption at +0.8 V, two new high-binding-energy features appear at 291.2 eV and 293.6 eV, assigned to CF_2 and CF_3 of the perfluoroalkyl chain, respectively, unequivocally evidencing PFOA on the surface [78]. Concomitantly, the original substrate components exhibit small positive shifts to 282.1, 284.2, 285.5, 286.3, and 288.4 eV, consistent with interfacial polarization/ligand effects [69]. However, their intensities decrease because the PFOA overlayer attenuates photoelectrons from the underlying carbon framework.

Fig. 7b shows the high-resolution O 1s spectra of MGL-3 before and after PFOA electroadsorption. Prior to adsorption, three components are observed at 529.8 eV (lattice M—O), 531.4 eV (surface —OH/Ti—OH), and 532.6 eV (adsorbed H_2O/weak oxygenates) [79]. After applying the adsorption bias, clear but small shifts and a redistribution of intensities occur, consistent with strong interaction of PFOA with the surface. The M—O peak remains essentially unchanged, shifting slightly to 530.0 eV and decreasing in relative intensity due to overlayer attenuation. Moreover, the carboxylate doublet shows at 531.6 eV (O═C—O^-) and 532.7 eV (C—O^-). This evolution, growth of the carboxylate pair at 531.6/532.7 eV together with the C 1s changes (O—C═O increase and CF_2/CF_3 at 291.2/293.6 eV), confirms surface binding of PFOA on MGL-3 [80]. This is consistent with carboxylate coordination at NiFe-LDH sites and/or anion exchange at positively charged LDH layers rather than any change to the lattice oxide [81].

Moreover, the Ni 2p spectra of the MGL-3 electrode before and after electroadsorption of the PFOA is shown in Fig. 7c. Before adsorption, MGL-3 shows a Ni^{2+}-type envelope with Ni $2p_{3/2}$ 856.1 eV and its satellite at 862.2 eV. Additionally, Ni $2p_{1/2}$ shows peak at 873.6 eV with a satellite at 880.0 eV [82]. After PFOA electroadsorption, the same Ni^{2+} pattern is retained but shifts slightly to higher binding energy, due to the ligand/polarization effects rather than redox. Thus, Ni 2p supports carboxylate coordination of PFOA to Ni(OH) sites [81]. Furthermore, for Fe 2p spectra (Fig. 7d) before adsorption, MGL-3 exhibits a Fe^{3+}-dominant envelope with Fe $2p_{3/2}$ of 712.3 eV (satellite of 720.2 eV) and Fe $2p_{1/2}$ of 726.1 eV (satellite of 733.71 eV) [83]. After PFOA electroadsorption, the same Fe^{3+} pattern is retained but shifts slightly to higher binding energy.

Furthermore, electrostatic forces are a key driver of electroadsorption. At pH > 7, MGL-3 under open circuit is negatively charged, which repels the anionic PFOA and diminishes adsorption (Fig. 4a). Applying a positive bias overcomes this repulsion and continuously draws $PFOA^-$ to the surface. For example, at pH 10 the MGL-3 at +0.8 *V* achieved a PFOA removal efficiency 37.1% higher than the open-circuit case. Beyond electrostatic enrichment and anion exchange, hydrogen bonding likely assists PFOA retention on MGL-3. The —COO^- headgroup can accept H-bonds from surface —OH on NiFe-LDH and Ti—OH on the MXene, often via a thin layer of interfacial water [81]. Furthermore, the ionic-strength experiments support that electrostatic interactions are a driver of PFOA electroadsorption on MGL-3. Increasing $NaNO_3$ from 1 to 10 mM reduces removal under closed-circuit conditions from 94.33% to 73.93% and under open-circuit conditions from 78.02% to 60.49%, as shown in Fig. 4b. This is consistent with compression of the electric double layer and increased competition of background anions for positively charged LDH-associated adsorption environments [55]. The consistently higher removal under bias across the full ionic-strength range confirms that the applied potential enhances uptake by continuously enriching $PFOA^-$ at the positively polarized interface.

Therefore, electrostatic enrichment under bias, together with competitive anion effects at LDH sites, explains the strong dependence on electrolyte concentration. Moreover, Fig. 8 shows the schematic diagram of the electroadsorption of the PFOA in the MGL-3.

4. Conclusion

MXene@rGO (MG) and MXene@rGO–NiFe-LDH (MGL) electrodes were developed and benchmarked for PFOA electroadsorption under identical conditions, where the ternary MGL architecture consistently outperformed the binary control. The optimized MGL-3 electrode combines a highly accessible porous sheet network (BET: 255.4 $m^2\ g^{-1}$ vs 28.7 $m^2\ g^{-1}$ for MG-10 and 17.5 $m^2\ g^{-1}$ for MXene) with improved charge/ion transport ($R_s = 0.78\ \Omega$ vs 1.21 Ω and 1.79 Ω), enabling faster interfacial charging and stronger electrosorption. Moreover, electrochemical analyses (CV/GCD/EIS) indicate quasi-rectangular EDL behavior and a predominantly surface-controlled charge-storage process, with the capacitive contribution increasing from 59.6% to 80.4% as scan rate rises from 0.2 to 1.0 mV s^{-1}. In electrosorption tests, MGL-3 achieved the highest removal under modest bias (+0.8 V) and maintained strong performance over a wide pH range (98.45% at pH 4 and 86.39% at pH 10). Additionally, electrolyte effects revealed an optimum at 1 mM $NaNO_3$ (94.33% removal), with decreased efficiency at higher ionic strength (81.93% and 73.93% at 5 and 10 mM), consistent with competitive screening effects. The adsorption process follows pseudo-second-order kinetics, with MGL-3 exhibiting the fastest uptake (ν_o = 15.93 mg g^{-1} min^{-1}), while equilibrium is well described by the Langmuir model ($Q_{max} = 119.52$ mg g^{-1}), exceeding MG (91.59 mg g^{-1}) and MXene (64.55 mg g^{-1}). Finally, XPS confirms PFOA accumulation under applied potential and supports carboxylate-associated interactions on the electrode surface. Thus, the rGO spacing and NiFe-LDH functional layer synergistically reduce resistance, accelerate surface charging, and enhance adsorption capacity, positioning MGL-3 as a promising electroadsorbent for PFAS remediation at low operating potentials.

Declaration of competing interest

The authors declare that they have no known competing financial interests or personal relationships that could have appeared to influence the work reported in this paper.

Acknowledgments

This work was financially supported by the Zhejiang Provincial Basic and Public Welfare Research Program (No. LGF22B070001). The authors also express their gratitude to Princess Nourah bint Abdulrahman University Researchers Supporting Project number (PNURSP2026R81), Princess Nourah bint Abdulrahman University, Riyadh, Saudi Arabia.

Appendix A. Supplementary data

Supplementary data to this article can be found online at https://doi.org/10.1016/j.seppur.2026.137073.

Data availability

No data was used for the research described in the article.

References

[1] S.B. Fatima, H.U. Khan, A. Bibi, M. Hamza, R. Zahra, S.U. Rehman, A. Farooqi, Water scarcity impact on water quality and implications for residents in Islamabad, Pakistan, Environ. Earth Sci. 84 (2025) 563.
[2] F. Fatehi, E. Khalili Sadrabad, M. Feilizadeh, Z. Derakhshan, S. Heidari Kochaki, S. Hekmatimoghaddam, A. Jebali, F.A. Mohajeri, Designing the pH-sensitive indicator based on starch nanoparticle with bromocresol green for monitoring meat spoilage, Int. J. Environ. Health Res. 35 (2025) 1204–1212.
[3] J. Liu, D. Li, H. Chen, H. Wang, Y. Wada, M. Kummu, S.N. Gosling, H. Yang, Y. Pokhrel, P. Ciais, Timing the first emergence and disappearance of global water scarcity, Nat. Commun. 15 (2024) 7129.
[4] M. Rajan, D. Karunanidhi, J. Jaya, B. Preethi, T. Subramani, P. Aravinthasamy, A comprehensive review on human health hazards due to groundwater contamination: a global perspective, Phys. Chem. Earth, Parts A/B/C 135 (2024) 103637.
[5] A.S. Abouzied, A.B.M. Al, N.S. Alsaiari, S.A. Aldaghfag, M.A. Ismail, M. Karimov, A. Abduvokhidov, O. Mukhitdinov, I. Mahariq, Enhanced removal of per- and polyfluoroalkyl substances (PFAS) by NH_2-functionalized MOF with ex-situ grown layered double hydroxides: mechanistic insights and adsorption behavior, Sep. Purif. Technol. 382 (2026) 136051.
[6] S.Y. Wee, A.Z. Aris, Revisiting the "forever chemicals", PFOA and PFOS exposure in drinking water, npj clean, Water 6 (2023) 57.
[7] J. Yang, W. Pan, T. Chen, H. Feng, Y. Yan, Y. Tu, W. Li, S.A. Aldaghfag, A. Abilkasimov, R.A. Haggam, Visible-light-driven Z-scheme Cs2TiBr6–CaIn2S4 nanocomposites: interfacial charge transfer, band alignment, and dual photocatalytic activity toward CO2 conversion and degradation of PFAS compounds, J. Environ. Chem. Eng. 14 (2026) 121084.
[8] X. Lyu, F. Xiao, C. Shen, J. Chen, C.M. Park, Y. Sun, M. Flury, D. Wang, Per-and polyfluoroalkyl substances (PFAS) in subsurface environments: occurrence, fate, transport, and research prospect, Rev. Geophys. 60 (2022) e2021RG000765.
[9] I. Najm, B. Gallagher, N. Vishwanath, N. Blute, A. Gorzalski, A. Feffer, S. Richardson, Per-and polyfluoroalkyl substances removal with granular activated carbon and a specialty adsorbent: a case study, AWWA Water Sci. 3 (2021) e1245.
[10] L. Khazdooz, A. Zarei, A. Abbaspourrad, Synthesis of an anion exchange resin for enhanced PFAS adsorption in water treatment, RSC Applied Polymers 3 (2025) 885–896.
[11] N.A. Masters, B.A. Marron, A. Lau, W.G. Bailey, S.D. Richardson, C.L. Bellona, Investigation of PFAS rejection by closed-circuit reverse osmosis and nanofiltration and sorption to treatment materials during groundwater treatment: a pilot demonstration, Separation and Purification Technology 377 (2025) 134308.
[12] H.D.H. Nhu, D. Van Tri, T. Le Luu, J. Trippel, M. Wagner, Degradation of 29 per- and poly-fluoroalkyl substances (PFAS) in water using Fenton-assisted electrochemical oxidation process, Sep. Purif. Technol. 362 (2025) 131908.
[13] N. Wu, J. Yu, J. Yuan, Y. Lu, Y. Pang, X. Liu, J. Wang, A. Yu, W. Xiao, L. Tang, Per- and polyfluoroalkyl substances in the environment and their removal by advanced oxidation processes, Frontiers of, Environ. Sci. Eng. 19 (2025) 1–20.
[14] B. Topolovec, O. Jovanovic, N. Puac, N. Skoro, E.C. Lumbaque, M. Petrovic, Plasma water treatment for PFAS: study of degradation of perfluorinated substances and their byproducts by using cold atmospheric pressure plasma jet, J. Environ. Chem. Eng. 12 (2024) 112979.
[15] J. Yu, C. He, X. Liu, J. Wu, Y. Hu, Y. Zhang, Removal of perfluorinated compounds by membrane bioreactor with powdered activated carbon (PAC): adsorption onto sludge and PAC, Desalination 334 (2014) 23–28.
[16] Y. Zhang, Y. Luo, J. Tong, X. Liu, Y. Chen, T. Xu, Machine learning screening based strategy for the synthesis of a molecularly imprinted ionic liquid polymer for specific adsorption of perfluorooctanoic acid, Sep. Purif. Technol. 327 (2023) 124894.
[17] A. Zaggia, L. Conte, L. Falletti, M. Fant, A. Chiorboli, Use of strong anion exchange resins for the removal of perfluoroalkylated substances from contaminated drinking water in batch and continuous pilot plants, Water Res. 91 (2016) 137–146.
[18] L. Zhang, T. Chen, Y. Wang, X. Wei, Z. Yue, D. Bai, W. Zhao, S. Zhang, W. Zhang, Synthesis of olefin-linked high stability covalent organic frameworks for the removal of perfluoroalkyl acids from water, Sep. Purif. Technol. 338 (2024) 126476.
[19] E. Mousset, M. Fournier, X. Su, Recent advances of reactive electroseparation systems for water treatment and selective resource recovery, Curr. Opin. Electrochem. 42 (2023) 101384.
[20] N. Saeidi, F. Harnisch, V. Presser, F.-D. Kopinke, A. Georgi, Electrosorption of organic compounds: state of the art, challenges, performance, and perspectives, Chem. Eng. J. 471 (2023) 144354.
[21] J. Jeon, J. Elbert, C.-H. Chung, J. Chae, X. Su, Chiral metallopolymers for redox-mediated enantioselective interactions, Adv. Funct. Mater. 33 (2023) 2301545.
[22] J. Wang, X. Wei, W. Song, X. Shi, X. Wang, W. Zhong, M. Wang, J. Ju, Y. Tang, Plasmonic enhancement in water splitting performance for NiFe layered double hydroxide-N10TC MXene heterojunction, ChemSusChem 14 (2021) 1948–1954.
[23] H. He, Y. Chen, C. Yang, L. Yang, Q. Jiang, H. Huang, Constructing 3D interweaved MXene/graphitic carbon nitride nanosheets/graphene nanoarchitectures for promoted electrocatalytic hydrogen evolution, journal of energy, Chemistry 67 (2022) 483–491.
[24] I. Marouani, W.H. Hassan, N.S.S. Singh, M. Hasan, A. Abduvokhidov, M. Karimov, A. Abilkasimov, I. Mahariq, M.A. Diab, Preparation of a novel reusable 2D-MXene with flower-like LDH composite for ultra-high adsorption of Congo red and doxycycline: stability and environmental application, J. Water Process Eng. 76 (2025) 108288.
[25] Y. Shi, B. Li, Q. Zhu, K. Shen, W. Tang, Q. Xiang, W. Chen, C. Liu, J. Luo, S. Yang, MXene-based mesoporous nanosheets toward superior lithium ion conductors, Adv. Energy Mater. 10 (2020) 1903534.
[26] L. Zhang, Y. Han, M. Sun, F. Li, S. Li, T. Gui, Facile design of FeCu metal-organic frameworks anchored on layer Ti3C2Tx MXene for high-performance electrochemical sensing of resorcinol, Talanta 275 (2024) 126100.
[27] S. Li, Y. Jiang, J. Liang, L. Zhang, F. Li, X. Lv, Atomic doping resets the local electronic structure of a 2D V2C MXene-based heterointerface for efficient urea-

assisted alkaline water splitting, Journal of Colloid and Interface Science 704 (2026) 139476.
[28] L. Zhang, M. Liang, C. Li, F. Li, J. Xin, J. Lang, S. Li, D. Zhang, Tailoring MXene-heterometal-doped MOF composites via one-step room-temperature synthesis for enhanced electrochemical detection of L-tryptophan, Anal. Chem. 97 (2025) 7203–7211.
[29] J. Zhao, Y. Fan, J. Zhangle, C. Ni, Electrosorption approach removing PFOA from wastewater using a MXene-polyaniline film, J. Water Process Eng. 62 (2024) 105415.
[30] S. Anantharaj, K. Karthick, S. Kundu, Evolution of layered double hydroxides (LDH) as high performance water oxidation electrocatalysts: a review with insights on structure, activity and mechanism, materials today, Energy 6 (2017) 1–26.
[31] H. Liu, Z. Li, D. Kong, X. Chen, FeCN/MXene as novel heterogeneous electro-Fenton catalysts for the degradation of sulfathiazole: performance and mechanism investigation, J. Environ. Sci. 154 (2025) 300–313.
[32] R. Sharma, G.P. Bhat, S. Gandhi, MXene-rGO nanocomposite based electrochemical immunosensor for detection of endosulfan – an organochlorine pesticide, Chemosphere 370 (2025) 143997.
[33] S. Rajabi, Z. Derakhshan, A. Nasiri, M. Feilizadeh, A. Mohammadpour, M. Salmani, S.H. Kochaki, H. Shouhanian, H. Hashemi, Synergistic degradation of metronidazole and penicillin G in aqueous solutions using AgZnFe2O4@chitosan nano-photocatalyst under UV/persulfate activation, Environ. Technol. Innovation 35 (2024) 103724.
[34] A. Tsyganov, A. Shindrov, M. Vikulova, D. Zheleznov, A. Gorokhovsky, N. Gorshkov, Effect of LiCl electrolyte concentration on energy storage of supercapacitor with multilayered Ti3C2Tx MXene electrodes synthesized by hydrothermal etching, Processes 11 (2023) 2528.
[35] R.A. Chavan, G.P. Kamble, S.B. Dhavale, A.S. Rasal, S.S. Kolekar, J.-Y. Chang, A. V. Ghule, NiO@ MXene nanocomposite as an anode with enhanced energy density for asymmetric supercapacitors, Energy Fuel 37 (2023) 4658–4670.
[36] B. Gurzęda, N. Boulanger, A. Nordenström, C. Dejoie, A.V. Talyzin, Pristine MXene: in situ XRD study of MAX phase etching with HCl+ LiF solution, Adv. Sci. 11 (2024) 2408448.
[37] S.K. Abdel-Aal, A.I. Beskrovnyi, A.M. Ionov, R.N. Mozhchil, A.S. Abdel-Rahman, Structure investigation by neutron diffraction and x-ray diffraction of graphene nanocomposite CuO–rGO prepared by low-cost method, Phys. Status Solidi (a) 218 (2021) 2100138.
[38] A. Rundla, B. Kumar, P. Tripathi, P. Kumar, K. Singh, Ti3C2Tx MXene@ rGO composite electrodes for high-performance supercapacitor applications, J. Power Sources 632 (2025) 236408.
[39] B. Ma, F. Chen, Y. Cheng, X. Wang, S. Yan, R. Gong, H. Luo, Ti3C2Tx MXene@ NiFe layered double hydroxide derived multiple interfacial composites with efficient microwave absorption, J. Alloys Compd. 936 (2023) 168162.
[40] M. Mahmood, A. Rasheed, I. Ayman, T. Rasheed, S. Munir, S. Ajmal, P.O. Agboola, M.F. Warsi, M. Shahid, Synthesis of ultrathin MnO2 nanowire-intercalated 2D-MXenes for high-performance hybrid supercapacitors, Energy Fuel 35 (2021) 3469–3478.
[41] Z. Ma, X. Zhou, W. Deng, D. Lei, Z. Liu, 3D porous MXene (Ti3C2)/reduced graphene oxide hybrid films for advanced Lithium storage, ACS Appl. Mater. Interfaces 10 (2018) 3634–3643.
[42] S. Chen, T.-F. Hu, Q. Zhang, J.-M. Hong, UV–annealing synthesis of sulfur-doped graphene for bisphenol a electrocatalytic degradation, Appl. Surf. Sci. 569 (2021) 151042.
[43] X. Ju, X. Feng, X. Duan, B. Cui, G. Huang, Y. Chen, X. Tong, Z. Yang, P. Guo, S. Xu, J.-W. Shi, Interfacial engineering of MXene-induced nanoflower-like LDH heterostructures for enhanced CO_2 capture, Separation and Purification Technology 385 (2026) 136443.
[44] C. Casiraghi, A. Hartschuh, H. Qian, S. Piscanec, C. Georgi, A. Fasoli, K. S. Novoselov, D.M. Basko, A.C. Ferrari, Raman spectroscopy of graphene edges, Nano Lett. 9 (2009) 1433–1441.
[45] C. Yang, Q. Jiang, H. Huang, H. He, L. Yang, W. Li, Polyelectrolyte-induced Stereoassembly of grain boundary-enriched platinum Nanoworms on Ti3C2Tx MXene nanosheets for efficient methanol oxidation, ACS Appl. Mater. Interfaces 12 (2020) 23822–23830.
[46] X.-P. Li, W.-K. Han, K. Xiao, T. Ouyang, N. Li, F. Peng, Z.-Q. Liu, Enhancing hydrogen evolution reaction through modulating electronic structure of self-supported NiFe LDH, Catal. Sci. Technol. 10 (2020) 4184–4190.
[47] H. Huang, Y. Wei, B. Shen, Y. Zhang, H. He, Q. Jiang, L. Yang, A.K. Nanjundan, J. Na, X. Xu, J. Zhu, Y. Yamauchi, Synthesis of multiple-twinned pd nanoparticles anchored on graphitic carbon nanosheets for use as highly-active multifunctional electrocatalyst in formic acid and methanol oxidation reactions, Adv. Mater. Interfaces 7 (2020) 2000142.
[48] A. Amiri, Y. Chen, C. Bee Teng, M. Naraghi, Porous nitrogen-doped MXene-based electrodes for capacitive deionization, Energy Storage Mater. 25 (2020) 731–739.
[49] S. Bellamkonda, M. Mamlouk, Durability and Degradation Analysis of CoFe2O4 Supported on Carbon Nitride Composites for Alkaline Oxygen Evolution Reaction, 2025.
[50] Z. Zeng, B.-A. Mei, G. Song, M. Hamza, Z. Yan, Q. Wei, H. Feng, Z. Zuo, B. Jia, R. Xiong, Physical interpretation of the electrochemical impedance spectroscopy (EIS) characteristics for diffusion-controlled intercalation and surface-redox charge storage behaviors, J. Energy Storage 102 (2024) 114021.
[51] Z. Yuan, L. Wang, D. Li, J. Cao, W. Han, Carbon-reinforced Nb2CTx MXene/MoS2 nanosheets as a superior rate and high-capacity anode for sodium-ion batteries, ACS Nano 15 (2021) 7439–7450.
[52] H. Zhang, F. Zhang, Y. Wei, Q. Miao, A. Li, Y. Zhao, Y. Yuan, N. Jin, G. Li, Controllable design and preparation of hollow carbon-based nanotubes for asymmetric supercapacitors and capacitive deionization, ACS Appl. Mater. Interfaces 13 (2021) 21217–21230.
[53] K.-U. Goss, The pKa values of PFOA and other highly fluorinated carboxylic acids, Environ. Sci. Technol. 42 (2008) 456–458.
[54] Z. Niu, Y. Wang, H. Lin, F. Jin, Y. Li, J. Niu, Electrochemically enhanced removal of perfluorinated compounds (PFCs) from aqueous solution by CNTs-graphene composite electrode, Chem. Eng. J. 328 (2017) 228–235.
[55] E. Ayranci, B.E. Conway, Adsorption and electrosorption at high-area carbon-felt electrodes for waste-water purification: systems evaluation with inorganic, S-containing anions, J. Appl. Electrochem. 31 (2001) 257–266.
[56] Y. Xiao, Y. Li, H. Yang, S. Rashid, N. Graham, W. Yu, The irreversible transformation of the molecular structure of humic acid during pH change and its effects on the formation of disinfection by-products, J. Hazard. Mater. 488 (2025) 137504.
[57] W. Wang, Z. Xu, X. Zhang, A. Wimmer, E. Shi, Y. Qin, X. Zhao, B. Zhou, L. Li, Rapid and efficient removal of organic micropollutants from environmental water using a magnetic nanoparticles-attached fluorographene-based sorbent, Chem. Eng. J. 343 (2018) 61–68.
[58] D. Liu, L. Zhou, Y. Liu, C. Xia, J. Ouyang, A.A. Adesina, Electrodeposition fabrication of graphene oxide/α-MnO2/polyaniline hierarchical porous electrodes with large hybrid specific capacitance for efficient U (VI) electrosorption, J. Environ. Chem. Eng. 12 (2024) 113450.
[59] L. Liu, D. Li, C. Li, R. Ji, X. Tian, Metal nanoparticles by doping carbon nanotubes improved the sorption of perfluorooctanoic acid, J. Hazard. Mater. 351 (2018) 206–214.
[60] S. Mohamed Nasser, M. Abbas, M. Trari, Understanding the rate-limiting step adsorption kinetics onto biomaterials for mechanism adsorption control, Prog. React. Kinet. Mech. 49 (2024) 14686783241226858.
[61] K.V. Kumar, S. Gadipelli, B. Wood, K.A. Ramisetty, A.A. Stewart, C.A. Howard, D. J. Brett, F. Rodriguez-Reinoso, Characterization of the adsorption site energies and heterogeneous surfaces of porous materials, J. Mater. Chem. A 7 (2019) 10104–10137.
[62] I. Ahmed, K.K. Adhikary, K. Kim, W.-S. Ahn, Aqueous adsorption of sulfamethoxazole on an N-doped zeolite beta-templated carbon, J. Colloid Interface Sci. 582 (2021) 467–477.
[63] Y. Chen, M. Li, Y. Li, Y. Liu, Y. Chen, H. Li, L. Li, F. Xu, H. Jiang, L. Chen, Hydroxyapatite modified sludge-based biochar for the adsorption of Cu2+ and Cd2+: adsorption behavior and mechanisms, Bioresour. Technol. 321 (2021) 124413.
[64] R. Wang, H. Zou, R. Zheng, X. Feng, J. Xu, Y. Shangguan, S. Luo, W. Wei, D. Yang, W. Luo, Molecular dynamics beyond the monolayer adsorption as derived from Langmuir curve fitting, Inorg. Chem. 61 (2022) 7804–7812.
[65] B. Shrestha, M. Ezazi, S. Seo, U. Sim, D.H. Lee, G. Kwon, Electrosorption-driven remediation of PFAS-contaminated water using a MXene nanosheet-PEDOT: PSS adsorbent, ACS Appl. Eng. Mater. 2 (2024) 368–375.
[66] Z. Yan, Y. Sun, J. Yan, R. Liu, J. Zhang, J. Song, Rapid adsorption of per-and polyfluoroalkyl substances (PFAS) on N-doped porous carbons (NPCs) derived from ZIF-8 over a wide pH range: adsorption behaviors and mechanisms, Sep. Purif. Technol. 365 (2025) 132575.
[67] Z. Wu, H. Zhong, X. Yuan, H. Wang, L. Wang, X. Chen, G. Zeng, Y. Wu, Adsorptive removal of methylene blue by rhamnolipid-functionalized graphene oxide from wastewater, Water Res. 67 (2014) 330–344.
[68] Q. Hu, Z. Zhang, Application of Dubinin–Radushkevich isotherm model at the solid/solution interface: a theoretical analysis, J. Mol. Liq. 277 (2019) 646–648.
[69] H. Lin, Y.-L. Feng, D. Lin, A.-G. Wang, A.Q. Zarifzoda, S. Zhou, F. Chen, G. Ying, Electrochemically enhanced adsorption of perfluorooctanoic acid (PFOA) on CuO-CNTs composite electrodes, Desalination 600 (2025) 118457.
[70] S. Yoon, J. Park, A.K.R. Police, J.K. Choe, S. Bae, Enhanced removal of perfluorooctanoic acid by aluminum-based metal–organic frameworks prepared by bauxite residue, J. Hazard. Mater. 483 (2025) 136687.
[71] S.S. Elanchezhiyan, J. Preethi, K. Rathinam, L.K. Njaramba, C.M. Park, Synthesis of magnetic chitosan biopolymeric spheres and their adsorption performances for PFOA and PFOS from aqueous environment, Carbohydr. Polym. 267 (2021) 118165.
[72] S. Kutsuna, H. Hori, T. Sonoda, T. Iwakami, A. Wakisaka, Preferential solvation of perfluorooctanoic acid (PFOA) by methanol in methanol–water mixtures: a potential overestimation of the dissociation constant of PFOA using a Yasuda–Shedlovsky plot, Atmos. Environ. 49 (2012) 411–414.
[73] S. Hu, K. Xie, X. Zhang, S. Zhang, J. Gao, H. Song, D. Chen, Significantly enhanced capacitance deionization performance by coupling activated carbon with triethyltetramine-functionalized graphene, Chem. Eng. J. 384 (2020) 123317.
[74] A. Saeed, M. Sharif, M. Iqbal, Application potential of grapefruit peel as dye sorbent: kinetics, equilibrium and mechanism of crystal violet adsorption, J. Hazard. Mater. 179 (2010) 564–572.
[75] J. Huang, A.B.M. Ali, S. Samad, A. Abdulrahman, H. Osman, D. Jumanazarov, F. Atamurotov, I. Mahariq, Sustainable and Electrostatically Engineered MXene-Based composite for environmental pollution remediation of Congo red dye and Cefixime from wastewater, Separation and Purification Technology 369 (2025) 133164.
[76] I. Marouani, Waqed H. Hassan, Narinderjit Singh Sawaran Singh, Mudassir Hasan, Alisher Abduvokhidov, Mukhtorjon Karimov, Akmal Abilkasimov, Ibrahm Mahariq, M.A. Diab, Preparation of a novel reusable 2D-MXene with flower-like LDH composite for ultra-high adsorption of Congo red and doxycycline: stability and environmental application, journal of water, Process. Eng. 26 (2025) 108288.

[77] V. Natu, M. Benchakar, C. Canaff, A. Habrioux, S. Célérier, M.W. Barsoum, A critical analysis of the X-ray photoelectron spectra of Ti3C2Tz MXenes, Matter 4 (2021) 1224–1251.
[78] L. Liu, Y. Liu, C. Li, R. Ji, X. Tian, Improved sorption of perfluorooctanoic acid on carbon nanotubes hybridized by metal oxide nanoparticles, Environ. Sci. Pollut. Res. 25 (2018) 15507–15517.
[79] H. Zhang, M. Li, N. Li, R. Jiang, E. Yin, X. Li, Performance enhancement and mechanism of tetracycline removal by visible light-driven photo bio-electro-Fenton system with CoFe-LDH/g-C3N4 cathode, J. Environ. Manag. 384 (2025) 125526.
[80] Y. Guo, Z. Li, W. Li, X. Chen, Z. Cai, Hydrophobic SERS substrate for PFOA sensing and cooperative adsorption, Talanta 294 (2025) 128244.
[81] L. Liu, Y. Liu, N. Che, B. Gao, C. Li, Electrochemical adsorption of perfluorooctanoic acid on a novel reduced graphene oxide aerogel loaded with cu nanoparticles and fluorine, J. Hazard. Mater. 416 (2021) 125866.
[82] Z. Qiu, C.-W. Tai, G.A. Niklasson, T. Edvinsson, Direct observation of active catalyst surface phases and the effect of dynamic self-optimization in NiFe-layered double hydroxides for alkaline water splitting, Energy Environ. Sci. 12 (2019) 572–581.
[83] H. Wang, T. Zhou, P. Li, Z. Cao, W. Xi, Y. Zhao, Y. Ding, Self-supported hierarchical nanostructured NiFe-LDH and Cu3P weaving mesh electrodes for efficient water splitting, ACS Sustain. Chem. Eng. 6 (2018) 380–388.